

Crystalline and dielectric properties of sputter deposited PbTiO₃ thin films

Ø. Dahl, J. K. Grepstad, and T. Tybell^{a)}*Department of Electronics and Telecommunications, Norwegian University of Science and Technology, O.S. Bragstads plass 2a, NO-7491 Trondheim, Norway*

(Received 14 November 2007; accepted 30 March 2008; published online 12 June 2008)

The crystalline and dielectric properties of sputter deposited PbTiO₃ thin films were investigated as a function of the film thickness and growth temperature. The crystalline quality was found to be independent of the film thickness from 2.4 to 200 nm. The capacitance of 0.12 mm² Pt/PbTiO₃/SrRuO₃ and Pt/PbTiO₃/Nb:SrTiO₃ capacitors was found to deviate from the ideal parallel plate capacitance for PbTiO₃ films thinner than 10 nm. The decrease in capacitance was consistent with field penetration into the electrodes. The surface Pb content, as determined from x-ray photoelectron spectroscopy, was found to decrease with increasing growth temperature from 700 to 760 °C. However, no change could be observed in the crystalline quality. © 2008 American Institute of Physics. [DOI: 10.1063/1.2937251]

I. INTRODUCTION

When ferroelectric and related high dielectric constant materials are processed in thin film form, the dielectric constant generally decreases with decreasing film thickness.¹ The low frequency dielectric constant is commonly measured via the capacitance of parallel plate type capacitors, and the observed reduction in the dielectric constant is often rationalized in terms of an interfacial layer with low dielectric constant in series with the bulk dielectric. Such an interfacial layer is found in theoretical models of the polarization, where the loss of dipole-dipole interactions at the film surface results in a reduced dielectric constant.^{2,3} In addition, the series capacitance associated with electric field penetration into the metal electrodes will also reduce the measured capacitance from the ideal parallel plate capacitor value.^{4,5} However, the microstructure of the thin film will affect the dielectric properties, and it is hard to separate the influence of thickness dependent variations in the microstructure on the dielectric constant from intrinsic thickness variations of the dielectric constant.

In particular, several studies on the dielectric properties of PbZr_xTi_{1-x}O₃ (PZT) films have reproduced the general thickness dependence.⁶⁻⁹ Most of the data reported in literature, however, derives from polycrystalline films. Fujisawa *et al.*¹⁰ found less thickness variation of the dielectric constant for epitaxial compared with polycrystalline PZT films. Recently, Pintilie *et al.*¹¹ reported dielectric measurements on epitaxial PZT films. They concluded that the decrease in the dielectric constant with decreasing film thickness was an artifact of the traditional analysis in terms of a parallel plate capacitor. Moreover, in their analysis, the intrinsic dielectric constant was close to the measured value in fully depleted thin films, and the increase in the dielectric constant with increasing film thickness was attributed to a leaky bulk region of the film.

Furthermore, the ferroelectric properties of PZT are known to vary with cation stoichiometry. For instance, the

Curie temperature¹² and remanent polarization^{13,14} have both been found to decrease with decreasing Pb content. With the use of Pb-enriched sources, however, it is possible to grow near stoichiometric PZT thin films.¹⁵⁻²⁰

In this paper, we investigate the influence of the film thickness on the crystalline and dielectric properties of rf-magnetron sputter deposited PbTiO₃ (PTO) thin films. The growth temperature dependence of the cation stoichiometry and the consequences for the crystalline quality and dielectric properties are also assessed.

II. EXPERIMENTAL DETAILS

A. Sample growth

The samples investigated in this study were grown on (i) insulating SrTiO₃ (STO) substrates, (ii) conductive Nb-doped (0.5 wt %) SrTiO₃ (Nb:STO) substrates, and (iii) SrRuO₃ (SRO) films deposited *in situ* on STO substrates. All substrates were (001) oriented, with a miscut angle of less than 0.1°. Commercially available annealed (Nb:STO) or HF-etched and annealed (STO) substrates were used.

The PTO films were grown by off-axis rf-magnetron sputtering from a nonstoichiometric target with 10% excess Pb. All samples were grown with an Ar:O₂ ratio of 10:4 and a total pressure of 165 mTorr. The sputtering power was 90 W, which gave a growth rate of ~0.2 nm/min. The samples were allowed to cool to room temperature in the growth ambient.

In order to study the impact of film thickness on the structural and dielectric properties, films with thicknesses ranging from 2.4 to 200 nm were grown. Two sets of PTO films were grown at substrate heater temperatures of 725 and 735 °C, respectively. To study the effect of growth temperature on the crystalline and dielectric properties, films with a thickness of 20 nm, sufficiently thick to display bulklike crystalline properties, were grown at substrate heater temperatures from 700 to 760 °C.²¹

The SRO layer was grown with an Ar:O₂ ratio of 10:4, a total pressure of 100 mTorr, and a sputtering power of 100 W. The layer thickness was 65 nm with a resistivity of

^{a)}Electronic mail: thomas.tybell@iet.ntnu.no.

$\sim 500 \mu\Omega \text{ cm}$. For measurements of the dielectric properties, circular Au/Pt contact pads with a diameter of 0.4 mm were deposited by e-beam evaporation through a stencil mask. The Nb:STO substrates and SRO films were used as bottom electrodes for the electrical characterization.

B. Structural characterization

The crystalline structure of the thin films was investigated with x-ray diffraction (XRD) using $\text{Cu } K\alpha$ ($\lambda = 0.15406 \text{ nm}$) radiation. The out-of-plane lattice constant and the film thickness were estimated from graphical comparisons of experimental and calculated diffraction patterns of the (001) and (002) diffraction peaks. The diffraction patterns were calculated from an idealized structure of N_{PTO} unit cells of PTO and N_{SRO} unit cells of SRO on a semi-infinite STO substrate.²² The structure factor for PTO was calculated from the bulk structure²³ but with the in-plane a -axis lattice constant set equal to the STO substrate value²³ (0.3905 nm) and the out-of-plane c -axis lattice constant used as a fitting parameter. The Ti and O displacements were scaled with the c -axis lattice constant. It has been shown that thin films of SRO grown on STO are compressively strained.²⁴ Taking into account the resulting expansion of the bulk orthorhombic unit cell in the out-of-plane (110) direction, a simplified tetragonal structure with 1 f.u./unit cell was used in the structure factor calculations for SRO. The in-plane lattice constant was set equal to the substrate value and the out-of-plane lattice constant used as a fitting parameter, as was done for the PTO structure factor.

To evaluate the crystalline quality of the PTO films, rocking curves were measured around the (001) and (002) diffraction peaks. In-plane coherence with the substrate was assessed from reciprocal space maps (RSM) of the (103) diffraction peak and pole figures of the (103) STO and (113) PTO diffraction peaks. The pole figures were measured with a 2θ angle corresponding to the (113) PTO peak ($\sim 77.0^\circ$), which is close to the (103) STO peak ($2\theta = 77.2^\circ$). The sample was rotated around the surface normal (the ϕ angle) and about an axis perpendicular to the surface normal (the θ angle).

The relative Pb:Ti ratio was measured with x-ray photoelectron spectroscopy (XPS). The recorded spectra were smoothed with a Sawitzky-Golay filter (11 points, fourth order) and fitted to Voigt functions and a Shirley background using a least squares algorithm. The relative integrated intensities of the XPS peaks were estimated from the fitted curves.

C. Dielectric characterization

Dielectric properties were measured with an Aixacrt TF analyzer 2000. The capacitance was measured on as-grown films at 2 kHz with a bias voltage of $\pm 0.1 \text{ V}$ and a small signal amplitude of 50 mV. The reported capacitances are average values over the bias range. The polarization was measured using a variant of the built-in dynamic hysteresis measurement procedure by the TF analyzer 2000.²⁵ Asymmetric triangular bipolar voltage pulses were used instead of the standard symmetric pulses to avoid large leakage currents at negative bias without decreasing the polarization field for

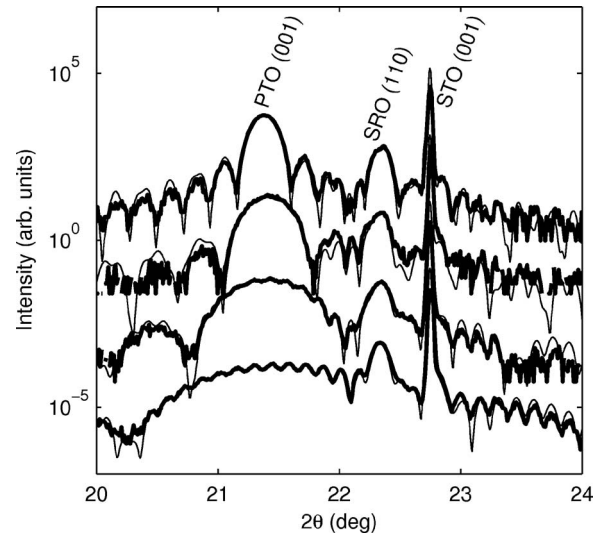


FIG. 1. $\theta/2\theta$ XRD scans of PTO grown on SRO/STO. The PTO film thickness was (from bottom to top) 7, 14, 24, and 41 nm, respectively. The diffractograms have been displaced along the intensity axis for clarity. Bold lines show measured data, while the fine lines are fits obtained from the idealized structure.

positive bias. Four pulses were applied, the first two pulses starting with negative half-periods and the final two pulses starting with positive half-periods. The positive half-period of the second pulse and the negative half-period of the fourth pulse were used to calculate the polarization. The pulse length was 1 ms with a dwell time of 2 ms between pulses. The positive and negative amplitudes were set independently, keeping a constant slew rate for the pulse. The polarization was calculated by integrating the measured current, including possible contributions from the leakage current. The voltage was defined as positive when applied to the top electrode.

III. RESULTS AND DISCUSSION

A. Influence of film thickness

1. Crystalline properties

Figure 1 shows typical XRD scans measured around the (001) diffraction peak along with calculated scans for the idealized structure.

The PTO film thicknesses were (from bottom to top) 7, 14, 24, and 41 nm, respectively. Thickness fringes around the (001) and (002) diffraction peaks could be readily observed in all but the thickest samples ($> 100 \text{ nm}$).

The c -axis lattice constant is plotted versus film thickness in Fig. 2. Four different sample series are shown: films grown on insulating STO substrates, films grown on conductive Nb:STO substrates, films grown on SRO films at a nominal temperature of 725°C , and films grown on SRO films at a nominal temperature of 735°C . As can be seen, for films thicker than 20 nm the lattice constant is close to the bulk value of 0.4152 nm.²³ Thinner films show a gradual decrease in the lattice constant that is in agreement with the previous reports, wherein this decrease was attributed to a reduction in the spontaneous polarization in thin films.²⁶ Transmission electron microscopy (TEM) images have

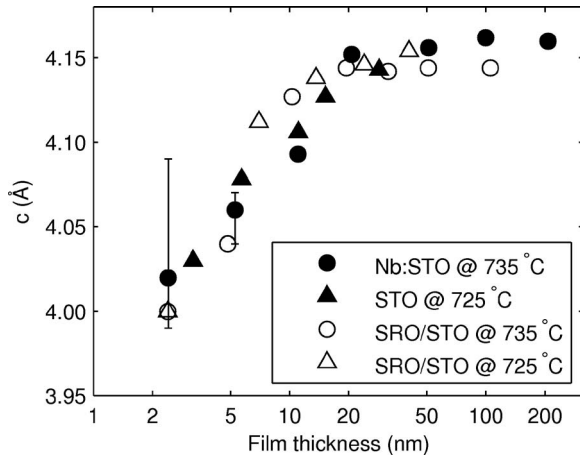


FIG. 2. The PTO c -axis lattice constant, as obtained from fits to the XRD data, plotted vs film thickness. Films thicker than 20 nm show a fixed out-of-plane lattice constant, close to the bulk value, while thinner films show a lattice constant which decreases monotonically with the film thickness. No significant difference is seen for films deposited on different substrates or grown at different substrate temperatures. The error bars, shown for films grown on Nb:STO substrates only, indicate the uncertainty in the fitted values. For films thicker than 10 nm, the error bars are smaller than the symbols.

shown a strained layer with a decreased c -axis lattice constant near the film/substrate interface,²⁷ recently observed also in PZT films for which a similar decrease in the lattice constant was found at the film/vacuum interface as well.²⁸ To a certain extent, the reduced c -axis lattice constant for very thin films, as measured with XRD, will be due to a growing contribution from the smaller c -axis lattice constant near the interfaces.

The full width at half maximum (FWHM) of rocking curves measured around the (001) PTO diffraction peak was typically twice that of the substrate, and less than 0.04° . In-plane epitaxy was maintained irrespective of thickness. The pole figure of the (113) PTO and (103) STO diffraction peaks in Fig. 3, for a 49 nm thick film grown on SRO/STO, shows the alignment of the in-plane lattice vectors of PTO and STO. The (113) PTO diffraction peaks appear at 45° with respect to the (103) STO diffraction peaks, which testifies to the cube on cube epitaxy. The reciprocal space map of the

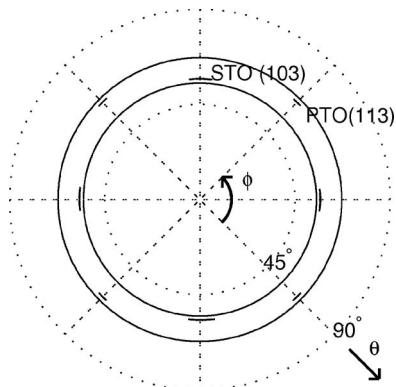


FIG. 3. Pole figure of the (113) PTO and (103) STO diffraction peaks for a 49 nm thick sample grown on SRO/STO. The solid circles identify the region of measurement. The (113) PTO peaks appear at 45° with respect to the (103) STO peaks, which testifies to the cube on cube epitaxy.

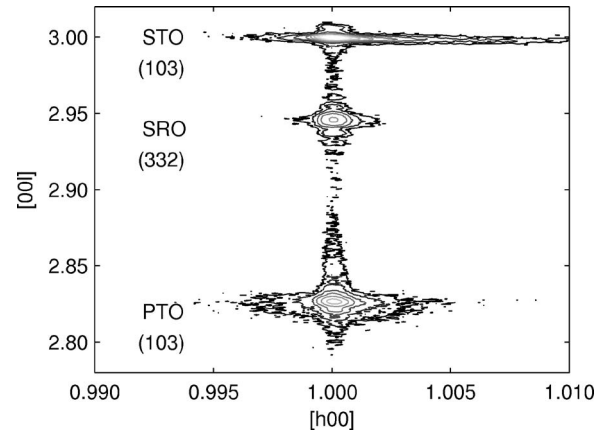


FIG. 4. Reciprocal space map of (103) diffraction peaks for a 100 nm thick PTO film grown on SRO/STO. The PTO, SRO, and STO peaks all have the same in-plane lattice constant.

(103) diffraction peak from a thick PTO film (100 nm) grown on SRO/STO in Fig. 4 shows that the in-plane lattice constants of SRO and PTO are both constrained to the substrate value.

Atomic force microscopy (AFM) imaging showed surfaces with a step-and-terrace structure that gradually disappears with increasing film thickness. The root-mean-square (rms) roughness on $5 \times 5 \mu\text{m}^2$ scans was measured at 0.2–0.9 nm. The change from a step-and-terrace structure to a homogeneous flat surface is illustrated in Fig. 5. The step-and-terrace structure is clearly seen for the thinner films, i.e., for (a) 5 nm, (b) 19 nm, and (c) 32 nm thick films. It degrades in the thicker films, (d) 41 nm and (e) 51 nm, and disappears entirely in (f) a 106 nm thick film. This trend was seen for films grown on both STO, Nb:STO, and SRO.

2. Dielectric properties

The measured capacitance of the Pt/PTO/SRO and Pt/PTO/Nb:STO structures is shown as a function of PTO film thickness in Fig. 6. For film thicknesses greater than 10 nm, the capacitance is proportional to the inverse thickness. In thinner films, a deviation from the inverse thickness dependence is seen for films grown with a SRO bottom electrode. Leakage currents prohibited measurements on films thinner than 4.5 nm. For films grown on a Nb:STO bottom electrode, the capacitance saturates at ~ 5 nF for thin films. A dielectric constant of $\epsilon_{\text{PTO}}/\epsilon_0 = 69$ was found from a fit to a linear thickness dependence of the inverse capacitance. For films with a Nb:STO bottom electrode, the fit was limited to films thicker than 10 nm. The clamped and free dielectric constants for PTO are 51 and 126, respectively, in single crystals.²³

It is known that field penetration into the electrodes will decrease the total capacitance of thin films.^{4,5} With two metal electrodes, the total inverse capacitance per unit area for a film of thickness d is

$$\frac{1}{C} = \left(\frac{\lambda_{\text{Pt}}}{\epsilon_{\text{Pt}}} + \frac{d}{\epsilon_{\text{PTO}}} + \frac{\lambda_{\text{SRO}}}{\epsilon_{\text{SRO}}} \right), \quad (1)$$

where λ_{Pt} and λ_{SRO} are free electron gas screening lengths for Pt and SRO in a linear dielectric background with dielec-

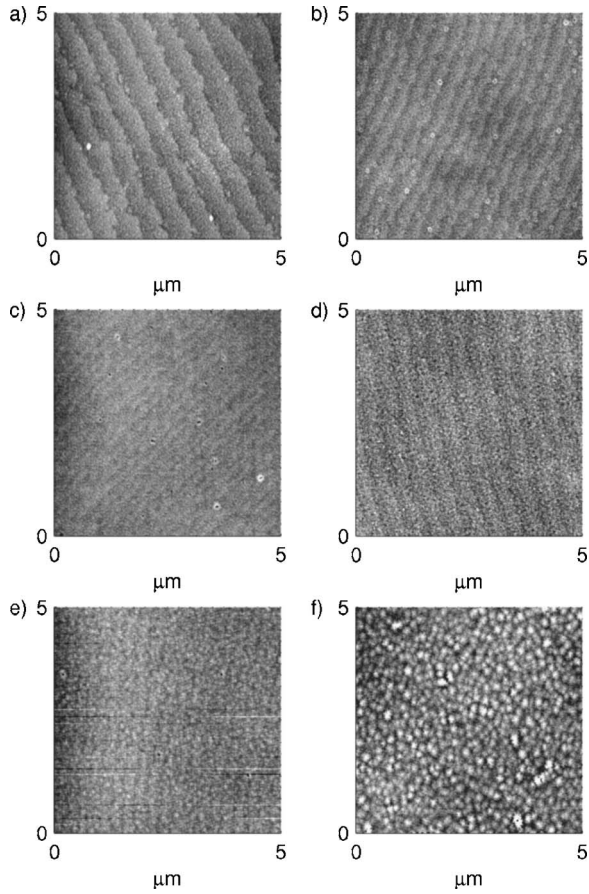


FIG. 5. AFM images of PTO films grown on SRO/STO. The film thicknesses were (a) 5 nm, (b) 19 nm, (c) 32 nm, (d) 41 nm, (e) 51 nm, and (f) 106 nm. The z -range of the linear grayscale is ± 1 nm for all images. Clear step-and-terrace structures are observed for the thinnest films, gradually disappearing for thicker films.

tric constants ϵ_{Pt} and ϵ_{SRO} , respectively.^{5,29} The screening lengths were estimated at $\lambda_{\text{Pt}}=0.06$ nm and $\lambda_{\text{SRO}}=0.11$ nm.³⁰ With these values, the expected series capacitance from the metal electrodes is 0.47 F/m². A fit to a linear thickness dependence of the inverse capacitance for films on SRO, shown in the inset of Fig. 6, actually gives a negative intercept of -3.90 ± 8.09 m²/F. The negative intercept can be interpreted in terms of an electrically short-circuited region with thickness of ~ 2 nm in the films. However, the upper limit of 4.2 m²/F gives a minimum experimental interface capacitance of 0.24 F/m², which can be interpreted in terms of an additional interface capacitance. Based on the estimated electrode capacitance, we find that any additional interface capacitance must be at least 0.48 F/m². The interface layers with strain normal to the interface, which were observed by TEM, could have a different dielectric constant from the bulk of the film, giving an additional interface capacitance. The capacitance from these strained layers can be expressed as

$$\frac{1}{C_{\text{inter}}} = d_{\text{inter}} \left(\frac{1}{\epsilon_{\text{inter}}} - \frac{1}{\epsilon_{\text{PTO}}} \right), \quad (2)$$

where d_{inter} and ϵ_{inter} are the total width and dielectric constant of the strained layers, respectively. Assuming that the strained layer width is ~ 1.8 nm at both the SRO and Pt

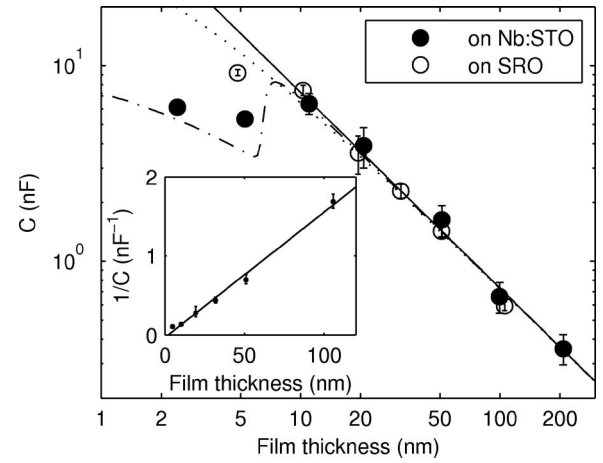


FIG. 6. Measured capacitance of Pt/PTO/Nb:STO capacitors (filled circles) and Pt/PTO/SRO capacitors (open circles) with 0.12 mm² area. The error bars are the standard deviations of measurements on different capacitors. The solid line is a fit to the data for films thicker than 10 nm, imposing an inverse thickness dependence. The dotted line is the capacitance calculated for an MIM model and the dash-dotted line is the capacitance calculated for an MIS model. The inset shows the inverse capacitance for films with an SRO bottom electrode vs. film thickness. The linear fit gives a negative intercept corresponding to -3.9 ± 8.1 m²/F.

interface, as was observed for an Nb:STO interface,²⁷ the dielectric constant in the strained layer does not decrease by more than 25% of the bulk value.

For films grown on Nb:STO, the total capacitance can be estimated from a metal-insulator-semiconductor (MIS) model,³¹ including the field-dependent dielectric constant of STO.^{32,33} The capacitance of the semiconductor surface is found following the analysis of Schottky diodes with field-dependent dielectric constants by Kahng and Wemple.³⁴ Treating the Nb:STO substrate as a nondegenerate semiconductor with bulk electron and hole densities n_0 and p_0 , the surface capacitance is found in the Appendix to be

$$C_s = -q n_0 \frac{p_0 (e^{-\beta\phi_s} - 1) - (e^{\beta\phi_s} - 1)}{E_s(\phi_s)}, \quad (3)$$

where q is the absolute value of the electron charge, $\beta = q/k_B T$ with k_B as Boltzmann's constant and T as the absolute temperature, and $E_s(\phi_s)$ and ϕ_s are the electric field and potential at the semiconductor/insulator interface, respectively. The potential is referenced to the bulk of the semiconductor. The interface potential will depend on the insulator thickness and the polarization, and is found numerically as described in the Appendix. With the small deviation of the dielectric constant in the strained interface layers, found for films with an SRO bottom electrode, the effect on the measured capacitance can be neglected. The total capacitance then is

$$\frac{1}{C} = \left(\frac{\lambda_{\text{Pt}}}{\epsilon_{\text{Pt}}} + \frac{d}{\epsilon_{\text{PTO}}} + \frac{1}{C_s} \right). \quad (4)$$

The result from the numerical calculations is shown as the dot-dash line in Fig. 6. It was assumed that the work function for Pt is $q\Phi_m=5.5$ eV,³⁵ the electron affinity for STO is $q\chi_s=4.0$ eV,³⁶ the bandgap of STO is $E_g=3.2$ eV,³⁷ and the

electron effective mass in STO is $m^*/m_e=10$.³⁸ The bulk electron density was assumed equal to the donor density $N_d=2 \times 10^{20} \text{ cm}^{-3}$ in the Nb:STO substrate, in accordance with carrier densities derived from transport measurements on similar substrates.³⁹ The polarization in the PTO film was assumed to be $-65 \mu\text{C}/\text{cm}^2$, the direction in agreement with our pyroelectric measurements, and the magnitude in reasonable agreement with the polarization measurements. As can be seen, the predicted capacitance is close to the ideal parallel plate value for thick films and significantly reduced for films thinner than ~ 10 nm. For thick films, the large negative polarization induces an inversion layer in the substrate surface, giving a large series capacitance. In thinner films, the potential difference of the electrodes opposes the formation of the inversion layer, and the small depletion layer capacitance dominates the total capacitance.

The film thickness at which this transition occurs can be estimated from a simplified model. Ignoring the free carrier density in depletion and weak inversion, the potential at the interface is³³

$$\phi_s = -\frac{\sqrt{ab}\epsilon_0}{qN_d} \left[\cosh\left(\frac{qN_d w}{b\epsilon_0}\right) - 1 \right], \quad (5)$$

where $a=1.64 \times 10^{15} (\text{V/m})^2$, $b=1.42 \times 10^{10} \text{ V/m}$, and w is the depletion layer width. Furthermore, $\phi_s = -E_g/q$ at strong inversion, so the depletion width is

$$w_c = \frac{b\epsilon_0}{qN_d} \operatorname{arcosh}\left(\frac{N_d E_g}{\sqrt{ab}\epsilon_0} + 1\right). \quad (6)$$

The transition occurs for the film thickness where the depletion layer just reaches this width, and this film thickness is found from the continuity of the displacement field at the interface as

$$d_c = \frac{\epsilon_i [\Phi_m - \chi_s - E_g/q - (qN_d \lambda_{PI} / \epsilon_{PI}) w_c]}{P_r + qN_d w_c}. \quad (7)$$

This thickness depends critically on the polarization. For a polarization between -60 and $-70 \mu\text{C}/\text{cm}^2$, which are plausible values for PTO, the critical thickness varies from 10 to 5 nm, in agreement with the experimental data.

B. Influence of growth temperature

1. Crystalline properties

The c -axis lattice constant was found to decrease with increasing growth temperature. Figure 7 shows a similar decrease for films grown on both Nb:STO and SRO. RSMs of the (103) diffraction peak showed no relaxation of the in-plane lattice constant, regardless of the growth temperature. Furthermore, the crystalline quality, as judged by the FWHM of the (001) rocking curve (less than 0.03°), was unaffected by the growth temperature. Figure 8 shows a $\theta/2\theta$ scan of a 53 nm thick film grown on Nb:STO at 735°C . The predominant peaks in this diffractogram are the PTO and STO (00l) diffraction peaks. In addition, a minor diffraction peak at $2\theta=45^\circ$ is attributed to an unidentified impurity phase. This peak was found in diffractograms recorded for 20 nm thick samples as well. The relative peak intensity of the impurity phase to the PTO (002) diffraction peak did not change with

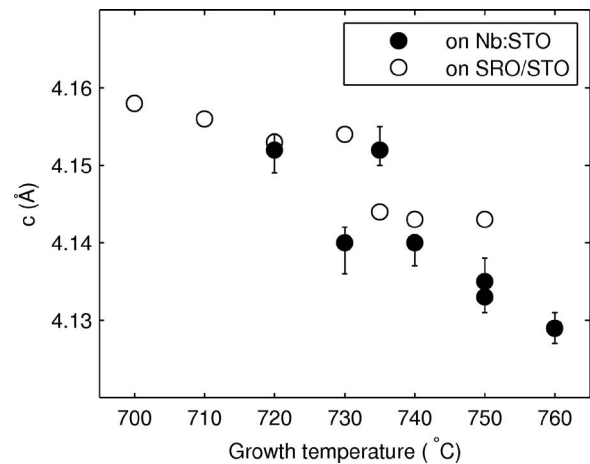


FIG. 7. The c -axis lattice constant for 20 nm thick films grown on Nb:STO (filled circles) and SRO (open circles) as a function of growth temperature. The error bars, shown for films grown on Nb:STO substrates only, indicate the uncertainty in the fitted values.

the growth temperature or with film thickness, suggesting that the volume fraction of the impurity phase is constant. The PTO film surfaces were flat, with a step-and-terrace structure. Rms values for the roughness, measured by AFM on $5 \times 5 \mu\text{m}^2$ scans, varied from 0.2 to 0.7 nm.

Quantitative XPS measurements of the Pb 4f and Ti 2p emission showed that the growth temperature affects the material composition. Figure 9 shows the Pb:Ti intensity ratio from measurements made on films grown on Nb:STO. It appears that the Pb:Ti ratio decreases with increasing growth temperature. The concomitant decrease in the lattice constant is consistent with the earlier reports.^{12,40}

2. Dielectric properties

Capacitance measurements on PTO films with SRO bottom electrodes gave a relative dielectric constant of 91 ± 13 , independent of the growth temperature, and in agreement with the dielectric constant found for the thickness series. The films were all ferroelectric irrespective of the growth temperature. Polarization hysteresis loops are shown in Fig.

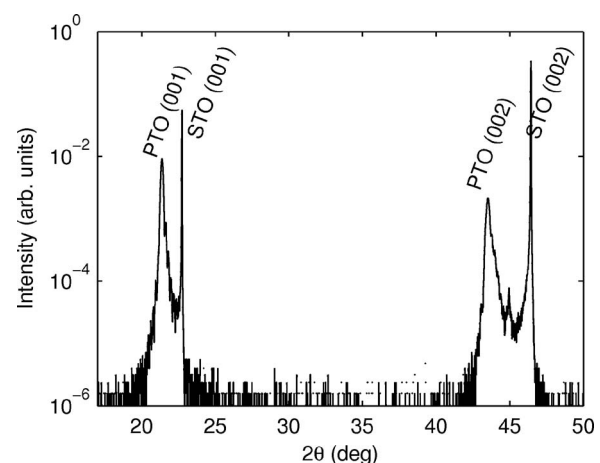


FIG. 8. $\theta/2\theta$ scan of a 53 nm thick PTO film grown on Nb:STO substrate at 735°C . The (00l) peaks from PTO and STO is seen along with an unidentified impurity phase at $2\theta \sim 45^\circ$.

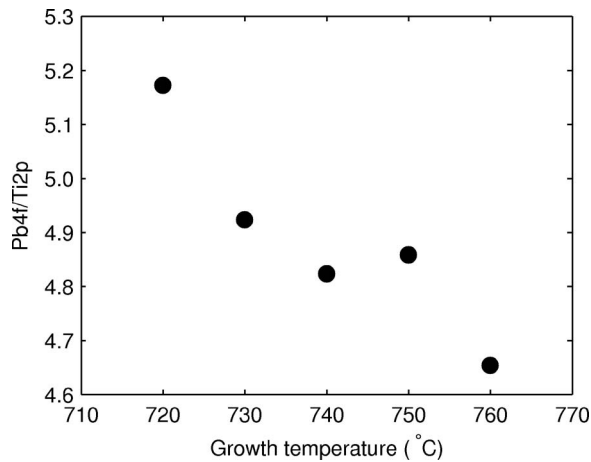


FIG. 9. Peak intensity ratio of the Pb 4*f* and Ti 2*p* emission from XPS measurements on PTO films on Nb:STO substrates, as a function of growth temperature. The relative Pb content is seen to decrease with increasing temperature.

10, together with the switching currents. All samples showed asymmetric hysteresis loops shifted toward a positive field. The maximum applied field was limited by an exponentially increasing leakage current with applied bias voltage. For a negative bias, this limiting field was 440–600 kV/cm, while positive bias permitted an applied field of 780–930 kV/cm. The negative field limit was found to decrease with increasing growth temperature. These upper and lower bounds on the bias voltage lead to unsaturated polarization loops. Samples grown at low temperatures, 700 °C (a) and 710 °C (b), showed a saturated polarization for negative fields and unsaturated polarization for positive fields. At higher growth temperatures, the polarization is unsaturated for both positive

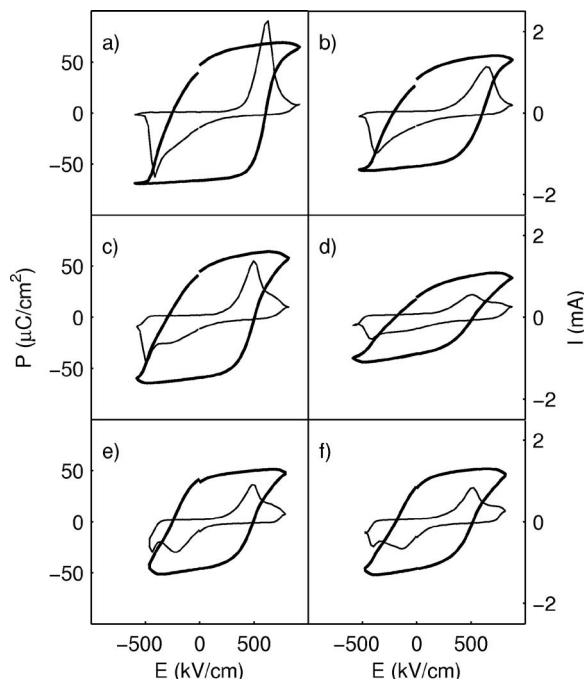


FIG. 10. Hysteresis loops (thick lines) and switching currents (thin lines) measured on PTO films with SRO bottom electrodes. The film growth temperatures were (a) 700 °C, (b) 710 °C, (c) 720 °C, (d) 730 °C, (e) 740 °C, and (f) 750 °C.

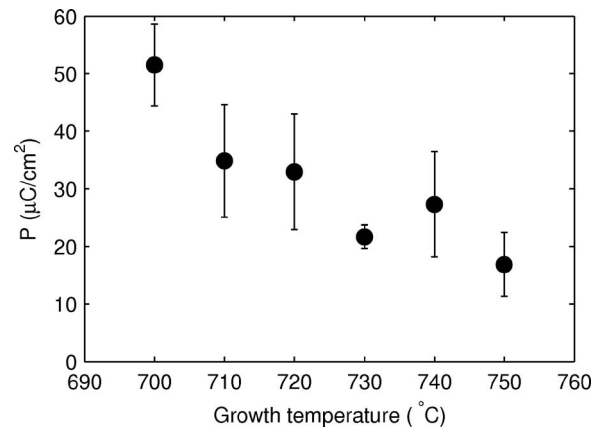


FIG. 11. Switchable polarization as a function of film growth temperature. A marked decrease in the polarization is seen with increasing growth temperature. The error bars are the standard deviations of measurements on different capacitors.

and negative fields. Moreover, the switching currents decreased in amplitude for samples grown at high temperatures. It remains unclear as to whether this is due to unsaturated polarization or derives from a decrease in spontaneous polarization.

The switchable polarization, defined as half the sum of the negative and positive polarization at zero field, is shown as a function of growth temperature in Fig. 11. Averaged over three to six contacts on each sample, the polarization varied from $51 \pm 7 \mu\text{C}/\text{cm}^2$ for a sample grown at 700 °C to $17 \pm 6 \mu\text{C}/\text{cm}^2$ for a sample grown at 750 °C. These polarization values are smaller than those estimated from the capacitance measurements on films with Nb:STO electrodes. This is attributed to the difference between the remanent polarization and the switchable polarization. For these unsaturated hysteresis loops, the switchable polarization can be less than the actual remanent polarization in the initial negative polarization state. The coercive field, defined as half the sum of the applied field at the switching current peaks, also decreased with growth temperature, from 474 ± 35 to 366 ± 55 kV/cm. The increase in leakage current with increasing growth temperature, which in PTO is often associated with Pb vacancies,⁴¹ is in agreement with the decreasing Pb content found from the XPS data.

IV. CONCLUSIONS

Good quality PTO films were grown with thicknesses from 2 to 200 nm. The crystalline quality was unaffected by the growth temperature from 700 to 760 °C. Films grown at high temperature appeared to be Pb deficient, as seen from unsaturated hysteresis loops, a reduced *c*-axis lattice constant, and a reduced Pb 4*f* to Ti 2*p* intensity ratio in XPS measurements.

Capacitance measurements were consistent with a thickness independent dielectric constant. The dielectric constant in the strained layer at the film/substrate interface previously observed in TEM images is not reduced by more than 25% compared with the bulk of the film.

ACKNOWLEDGMENTS

T.T. acknowledges support from the Research council of Norway under Grant No. 162874/V00.

APPENDIX: SURFACE CAPACITANCE OF SEMICONDUCTING ELECTRODE

The potential ϕ_s , at the semiconductor/insulator interface in the MIS model is found numerically from the continuity of the displacement field,

$$\epsilon_i E_i(\phi_s) + P_r = D_s(\phi_s), \quad (\text{A1})$$

where ϵ_i is the linear dielectric constant of the insulator, $E_i(\phi_s)$ is the electric field in the insulator (which, under the assumption of no free charge, is constant throughout the film), P_r is the remanent polarization in the insulator, and $D_s(\phi_s)$ is the displacement field in the semiconductor at the interface. The electric field in the insulator is

$$E_i(\phi_s) = -\frac{1}{d}[\Phi_m - \chi_s - \phi_m(\phi_s) + \phi_s], \quad (\text{A2})$$

where d is the insulator thickness, $q\Phi_m$ is the metal work function, $q\chi_s$ is the semiconductor electron affinity, and $\phi_m(\phi_s)$ is the potential at the metal-insulator interface referenced to the bulk of the semiconductor. It is assumed that the electron affinity is equal to the semiconductor work function. With an applied voltage V ,

$$\phi_m(\phi_s) = -\frac{\lambda_m}{\epsilon_m} D_s(\phi_s) + V, \quad (\text{A3})$$

where λ_m is the screening length and ϵ_m the dielectric constant of the metal. With the field-dependent dielectric constant of Nb:STO as found by Yamamoto *et al.*³³

$$\epsilon_{\text{STO}}(E) = \frac{b\epsilon_0}{\sqrt{a + E^2}}, \quad (\text{A4})$$

where the constants a and b are 1.64×10^{15} (V/m)² and 1.42×10^{10} V/m, respectively, the displacement field at the interface is

$$D_s(\phi_s) = \int_0^{E_s} \epsilon_{\text{STO}} dE = b\epsilon_0 \ln\left(\frac{E_s + \sqrt{a + E_s^2}}{\sqrt{a}}\right), \quad (\text{A5})$$

where $E_s = E_s(\phi_s)$ is the electric field in the semiconductor at the interface. The electric field is found using the standard textbook derivation,³¹ assuming nondegenerate carrier statistics, but allowing for a field dependent dielectric constant. The electric field is found as

$$E_s(\phi) = \pm \sqrt{\frac{1}{b^2} \left(\frac{k_B T}{qL_0}\right)^4 F^4(\phi) + 2 \frac{\sqrt{a}}{b} \left(\frac{k_B T}{qL_0}\right)^2 F^2(\phi)}. \quad (\text{A6})$$

The field is positive for positive ϕ and negative when ϕ is negative. The Debye-type length L_0 and the function $F(\phi)$ are³¹

$$L_0 = \sqrt{\frac{\epsilon_0}{qn_0\beta}} \quad (\text{A7})$$

and

$$F^2(\phi) = \frac{P_0}{n_0}(e^{-\beta\phi} + \beta\phi - 1) + (e^{\beta\phi} - \beta\phi - 1). \quad (\text{A8})$$

The assumption of nondegenerate carrier statistics for the 0.5 wt % Nb doped STO substrates is generally not applicable. However, the major effect of the film thickness and polarization dependence of the surface capacitance is from the depletion region, where the carrier density is described by nondegenerate statistics.

The capacitance of the surface layer is $C_s = \partial D_s / \partial \phi_s$, and is found from the the displacement field expressed as a function of surface potential ϕ_s ,

$$D_s(\phi_s) = -qn_0 \int_0^{\phi_s} \left[\frac{P_0}{n_0}(e^{-\beta\phi} - 1) - (e^{\beta\phi} - 1) \right] E^{-1}(\phi) d\phi. \quad (\text{A9})$$

Thus, the capacitance is

$$C_s = \frac{\partial D_s}{\partial \phi_s} = -qn_0 \frac{\frac{P_0}{n_0}(e^{-\beta\phi_s} - 1) - (e^{\beta\phi_s} - 1)}{E_s(\phi_s)}. \quad (\text{A10})$$

The flat-band capacitance is found from an expansion of the charge density and electric field for small ϕ_s to be

$$\lim_{\phi_s \rightarrow 0} C_s = \frac{qn_0 \sqrt{\frac{P_0}{n_0} + 1}}{\sqrt{\frac{a}{b}} \left(\frac{k_B T}{qL_0}\right)}. \quad (\text{A11})$$

¹T. M. Shaw, S. Trolier-McKinstry, and P. C. McIntyre, *Annu. Rev. Mater. Sci.* **30**, 263 (2000).

²C. Zhou and D. M. Newns, *J. Appl. Phys.* **82**, 3081 (1997).

³K. Natori, D. Otani, and N. Sano, *Appl. Phys. Lett.* **73**, 632 (1998).

⁴O. K. Rice, *Phys. Rev.* **31**, 1051 (1928).

⁵H. Y. Ku and F. G. Ullman, *J. Appl. Phys.* **35**, 265 (1964).

⁶T. Nakagawa, J. Yamaguchi, T. Usuki, Y. Matsui, M. Okuyama, and Y. Hamakawa, *Jpn. J. Appl. Phys.* **18**, 897 (1979).

⁷Y. Sakashita, H. Segawa, K. Tominaga, and M. Okada, *J. Appl. Phys.* **73**, 7857 (1993).

⁸K. Amanuma, T. Mori, T. Hase, T. Sakuma, A. Ochi, and Y. Miyasaka, *Jpn. J. Appl. Phys., Part 1* **32**, 4150 (1993).

⁹P. K. Larsen, G. J. M. Dormans, D. J. Taylor, and P. J. van Veldhoven, *J. Appl. Phys.* **76**, 2405 (1994).

¹⁰H. Fujisawa, S. Nakashima, K. Kaibara, M. Shimizu, and H. Niu, *Jpn. J. Appl. Phys., Part 1* **38**, 5392 (1999).

¹¹L. Pintilie, I. Vrejoiu, D. Hesse, G. LeRhun, and M. Alexe, *Phys. Rev. B* **75**, 224113 (2007).

¹²S.-i. Shirasaki, *Solid State Commun.* **9**, 1217 (1971).

¹³T. Mihara and H. Watanabe, *Jpn. J. Appl. Phys., Part 1* **34**, 5674 (1995).

¹⁴S. Aggarwal, S. Madhukar, B. Nagaraj, I. G. Jenkins, R. Ramesh, L. Boyer, and J. T. Evans, Jr., *Appl. Phys. Lett.* **75**, 716 (1999).

¹⁵K. Iijima, Y. Tomita, R. Takayama, and I. Ueda, *J. Appl. Phys.* **60**, 361 (1986).

¹⁶S. Ueno and H. Ishiwara, *Jpn. J. Appl. Phys., Part 1* **31**, 2982 (1992).

¹⁷G. J. M. Dormans, P. J. van Veldhoven, and M. de Keijser, *J. Cryst. Growth* **123**, 537 (1992).

¹⁸J. F. M. Cillessen, M. W. J. Prins, and R. M. Wolf, *J. Appl. Phys.* **81**, 2777 (1997).

¹⁹G. Velu and D. Remiens, *Vacuum* **56**, 199 (2000).

- ²⁰S. Aggarwal, K. R. Udayakumar, and J. A. Rodriguez, *J. Appl. Phys.* **100**, 064103 (2006).
- ²¹The substrate temperature, measured with an optical pyrometer at $1.55\ \mu\text{m}$, using an emissivity of 0.7, was 530–565 °C and 510–545 °C, as measured on Nb:STO and SRO substrates, respectively.
- ²²C. Thompson, C. M. Foster, J. A. Eastman, and G. B. Stephenson, *Appl. Phys. Lett.* **71**, 3516 (1997).
- ²³M. Adachi, J. Harada, T. Ikeda, S. Nomura, E. Sawaguchi, and T. Yamada, in *Group III: Crystal and Solid State Physics*, Landolt-Börnstein, New Series Vol. 16 edited by K.-H. Hellwege and A. M. Hellwege (Springer-Verlag, Berlin-Heidelberg, 1981).
- ²⁴C. B. Eom, R. J. Cava, R. M. Fleming, J. M. Phillips, R. B. van Dover, J. H. Marshall, J. W. P. Hsu, J. J. Krajewski, and W. F. Peck, Jr., *Science* **258**, 1766 (1992).
- ²⁵The standard procedure is described in the *TF analyzer 2000 FE-Module user manual* (aixACCT Systems GmbH, Aachen, Germany). In the standard procedure the positive and negative amplitudes are equal, and the dwell time between pulses is 1 s.
- ²⁶C. Lichtensteiger, J.-M. Triscone, J. Junquera, and P. Ghosez, *Phys. Rev. Lett.* **94**, 047603 (2005).
- ²⁷A. T. J. van Helvoort, Ø. Dahl, B. G. Soleim, R. Holmestad, and T. Tybell, *Appl. Phys. Lett.* **86**, 092907 (2005).
- ²⁸V. Nagarajan, J. Junquera, J. Q. He, C. L. Jia, R. Waser, K. Lee, Y. K. Kim, S. Baik, T. Zhao, R. Ramesh, Ph. Gosez, and K. M. Rabe, *J. Appl. Phys.* **100**, 051609 (2006).
- ²⁹R. R. Mehta, B. D. Silverman, and J. T. Jacobs, *J. Appl. Phys.* **44**, 3379 (1973).
- ³⁰The screening lengths were estimated from a carrier density for Pt of $6.6 \times 10^{23}\ \text{cm}^{-3}$, based on the lattice constant (Ref. 42) and assuming 10 conduction electrons per atom, and literature values of the carrier density for SRO of $1.22 \times 10^{22}\ \text{cm}^{-3}$ (Ref. 43), electron effective masses $m^*/m_e = 5$ for Pt and $m^*/m_e = 4$ for SRO (Refs. 44 and 45), a lattice dielectric constant $\epsilon_{\text{SRO}}/\epsilon_0 = 8.45$ for SRO (Ref. 46), and an assumed lattice dielectric constant of $\epsilon_{\text{Pt}}/\epsilon_0 = 10$ for Pt.
- ³¹S. M. Sze, *Physics of Semiconductor Devices*, 2nd ed. (Wiley, New York, 1981).
- ³²R. A. van der Berg, P. W. M. Blom, J. F. M. Cillessen, and R. M. Wolf, *Appl. Phys. Lett.* **66**, 697 (1995).
- ³³T. Yamamoto, S. Suzuki, H. Suzuki, K. Kawaguchi, K. Takahashi, and Y. Yoshisato, *Jpn. J. Appl. Phys., Part 2* **36**, L390 (1997).
- ³⁴D. Kahng and S. H. Wemple, *J. Appl. Phys.* **36**, 2925 (1965).
- ³⁵A. Goldmann, in *Group III: Condensed Matter*, Landolt-Börnstein, New Series Vol. 23 edited by W. Martienssen (Springer-Verlag, Berlin, 2003).
- ³⁶R. A. Powell and W. E. Spicer, *Phys. Rev. B* **13**, 2601 (1976).
- ³⁷J. A. Noland, *Phys. Rev.* **94**, 724 (1954).
- ³⁸H. P. R. Frederikse, W. R. Thurber, and W. R. Hosler, *Phys. Rev.* **134**, A442 (1964).
- ³⁹H. P. R. Frederikse and W. R. Hosler, *Phys. Rev.* **161**, 822 (1967).
- ⁴⁰C. D. Theis and D. G. Schlom, *J. Cryst. Growth* **174**, 473 (1997).
- ⁴¹J. P. Remeika and A. M. Glass, *Mater. Res. Bull.* **5**, 37 (1970).
- ⁴²W. G. Wyckoff, *Crystal Structures*, 2nd ed. (Interscience, New York, 1963), Vol. 1.
- ⁴³M. Shepard, S. McCall, G. Cao, and J. E. Crow, *J. Appl. Phys.* **81**, 4978 (1997).
- ⁴⁴D. L. Martin, *Phys. Rev. B* **17**, 1670 (1978).
- ⁴⁵P. A. Cox, R. G. Egdell, J. B. Goodenough, A. Hamnett, and C. C. Naish, *J. Phys. C* **16**, 6221 (1983).
- ⁴⁶D. J. Kim, J. Y. Jo, Y. S. Kim, Y. J. Chang, J. S. Lee, J.-G. Yoon, T. K. Song, and T. W. Noh, *Phys. Rev. Lett.* **95**, 237602 (2005).